RESEARCH ARTICLE

NANO · MICRO small
www.small-journal.com

Continuous Strain Modulation of Moiré Superlattice Symmetry From Triangle to Rectangle

*Hao Ou, Koshi Oi, Rei Usami, Takahiko Endo, Keisuke Shinokita, Ryo Kitaura, Kazunari Matsuda, Yasumitsu Miyata, Jiang Pu, and Taishi Takenobu**

Moiré superlattices formed in van der Waals (vdW) bilayers of 2D materials provide an ideal platform for studying previously undescribed physics, including correlated electronic states and moiré excitons, owing to the wide-range tunability of their lattice constants. However, their crystal symmetry is fixed by the monolayer structure, and the lack of a straightforward technique for modulating the symmetry of moiré superlattices has impeded progress in this field. Herein, a simple, room-temperature, ambient method for controlling superlattice symmetry is reported. The method uses vdW heterostructures on a flexible substrate; by bending the substrate, a uniaxial strain is introduced. Based on numerical calculations, a strain condition is designed to deform the moiré superlattice from triangular to rectangular, and visualized the continuous deformation of real-space moiré superlattices using piezoresponse force microscopy. The band calculations show that nearly flat moiré minibands remain in the rectangular lattice; therefore, this method provides an additional tuning knob for the Hamiltonian of moiré quantum matter.

1. Introduction

Stacking 2D van der Waals (vdW) monolayers with dissimilar lattice constants and/or slight rotational misalignment produces a moiré superlattice with a periodicity inversely related to the magnitude of the interlayer mismatch.[1,2] The length scale of the moiré period is typically several times larger than the atomic lattice constant (≈0.1 nm).[2] Importantly, the tunability of the lattice parameters in moiré materials is similar to that of quantum simulators based on ultracold gases, which are clean models using real physical systems to "simulate" quantum materials.[3,4] A difference in length scales of approximately one digit implies a complementary relationship between ultracold gases (≈100 nm) and moiré materials (≈1–100 nm). As such, moiré materials assembled from vdW layers are versatile platforms for simulating and designing the physics of electronic correlations and nontrivial band topology.[4–6] The tuning knobs required for quantum simulators, as realized in ultracold gases, are lattice constants and crystal symmetry.[7] In moiré materials, however, the controllability of the lattice symmetry is extremely limited, in stark contrast to the high tunability of lattice constants in ultracold gases.[4]

The limited symmetry of monolayers, which determines the superlattice symmetry, mostly limits moiré materials to honeycombs and triangles.[4] To obtain nonhoneycombs/triangles, a rectangular superlattice was theoretically proposed based on twisted bilayer (t-BL) germanium selenide,[8] and recently, it was demonstrated by t-BL of WTe_2/WSe_2.[9] Therefore, crystal symmetry is still not a tuning knob for moiré materials, and a method to control it other than material selection is urgently needed. In this study, we focused on the strain effect because the ultimate thinness of the monolayers allows intentional and continuous deformation by relatively weak forces, such as bending a plastic substrate. Although the effect of strain on moiré superlattices has already been thoroughly investigated from a theoretical viewpoint,[10–12] experimental reports have been limited to unintentional strain effects, and continuous control of the lattice constants and symmetry of moiré materials has not yet been achieved.[12–14] In this study, we demonstrated symmetry manipulation of moiré superlattices by continuous uniaxial deformation. We performed a piezoresponse force microscopy (PFM)

H. Ou, K. Oi, R. Usami, T. Takenobu
Department of Applied Physics
Nagoya University
Nagoya 464-8603, Japan
E-mail: takenobu@nagoya-u.jp
T. Endo, Y. Miyata
Department of Physics
Tokyo Metropolitan University
Tokyo 192-0397, Japan
K. Shinokita, K. Matsuda
Institute of Advanced Energy
Kyoto University
Kyoto 611-0011, Japan
R. Kitaura
Research Center for Materials Nanoarchitectonics (MANA)
National Institute for Materials Science (NIMS)
Tsukuba 305-0044, Japan
J. Pu
Department of Physics
Tokyo Institute of Technology
Tokyo 152-8551, Japan

The ORCID identification number(s) for the author(s) of this article can be found under https://doi.org/10.1002/smll.202407316

DOI: 10.1002/smll.202407316

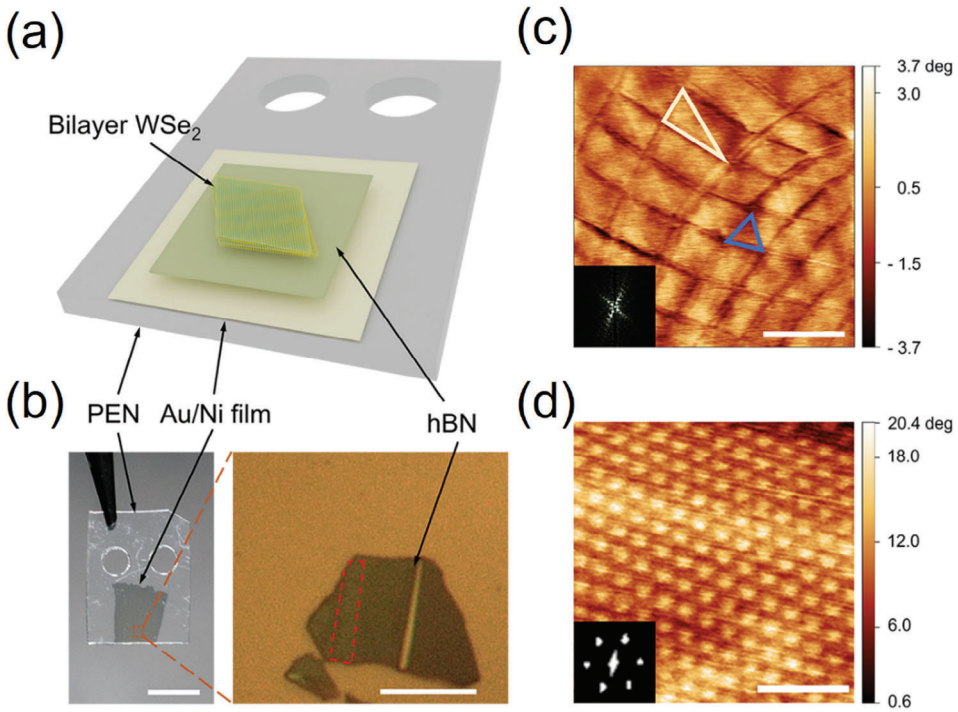

Figure 1. 2D vdW bilayer on plastic substrate. a) Schematic of the sample structure with twisted bilayer WSe_2 and hBN transferred on Au/Ni coated PEN substrate. b) Optical image of PEN substrate with Au/Ni film (left) and magnified microscopic image of the vdW stacking of sample #1 (right). The red dashed-line rectangle indicates the bilayer region. Scale bars: 5 mm (left), 20 µm (right). c) PFM amplitude image of sample #1, which shows clear long-period moiré patterns. Scale bar: 200 nm. Inset: Fast Fourier transform (FFT) image. d) PFM amplitude image of sample #2, which shows clear short-period moiré patterns. Scale bar: 50 nm. Inset: FFT image.

technique on a flexible plastic substrate to directly visualize intentionally deformed moiré superlattices. As an example of continuous tuning of the crystal symmetry, we realized a lattice symmetry alternation from triangular to rectangular. The calculated electronic band structures of the distorted moiré superlattices possess nearly flat moiré minibands and follow the continuously tunable Hubbard model, which is a major step toward the development of highly tunable quantum simulators based on moiré superlattices.

2. Results and Discussion

The uniaxial strain was applied to t-BL by simply bending the flexible substrate.[15–17] Although this is a well-established method, it is nearly impossible to visualize moiré superlattices on insulating plastic substrates using transmission electron microscopy[18] or scanning tunneling microscopy.[18,19] To solve this problem, we used the PFM method, which allows measurements of the insulating substrate in air.[9,13,20–22] The PFM technique resolves the moiré superlattice by leveraging the ferroelectricity or flexoelectricity inherent in stacked van der Waals heterostructures. In the measurement process, a conductive AFM cantilever is used to apply a voltage to the sample. The moiré-induced piezoelectric signal, which results from the strain induced in the material, is then detected through the deformation of the cantilever. Thanks to the high spatial resolution of AFM, it is possible to effectively resolve moiré superlattices with periodicities on the order of a few nanometers or even longer, allowing for the detailed analysis of the moiré pattern at the nanoscale level.[20]

Importantly, clear visualization of the moiré superlattice by PFM requires t-BL on the topmost surface of the flat sample. For a flat surface, we realized a strong interaction between the 2D vdW materials and plastic substrates using thin Au/Ni films on plastic substrates (see Figure S1 in the Supporting Information). For t-BL on the topmost surface, the commonly used "tear-and-stack" method, in which the top surface is hexagonal boron nitride (hBN), cannot be used.[1] Therefore, we adopted the dry pick-and-flip assembly technique established by Masubuchi et al., in which the topmost surface is a t-BL (**Figures 1a** and S2, Supporting Information).[23] As the target material, we selected single-crystalline triangular WSe_2 monolayers grown by the chemical vapor deposition (CVD) method (Figure S3, Supporting Information).[24] We fabricated t-BL WSe_2 on hBN and transferred it to a flexible polyethylene naphthalate (PEN) substrate, as shown in Figures 1a,b. To achieve a strong interaction between hBN and the substrate, we first deposited a thin Au/Ni film on the PEN substrate, as previous studies have reported strong adhesion between deposited metal films and van der Waals materials.[25,26] The lower surface roughness of the Au/Ni film compared to PEN helps enhance the van der Waals interaction between hBN and the substrate, resulting in a nearly flat sample surface.

Subsequently, we conducted PFM measurements (see the Experimental Section) and visualized the clear moiré superlattices. As illustrated in Figure 1c, the long-period (174 ± 43 nm)

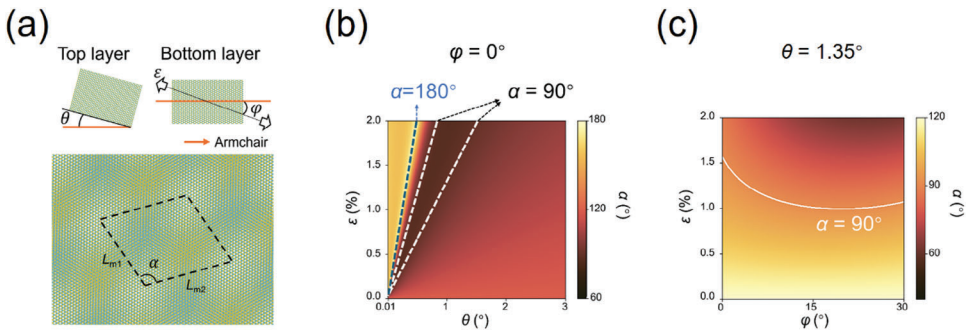

Figure 2. Calculated emergence of rectangular moiré superlattice. a) Schematic representation of the uniaxially strained twisted homobilayer. We assumed that the strain was uniaxial and applied it only to the bottom of the two monolayers. The parameter space spanned by the twist angle (θ), strain magnitude (ε), and strain angle (φ) determines the moiré pattern, which can be characterized by two moiré basis vectors (L_{m1} and L_{m2}) and the angle α between them. The orange arrow and lines indicate the armchair direction of the bottom layer. The black dashed parallelograms indicate the unit cell of the moiré superlattice. b) Variation of α as a function of twist angle and strain magnitude when the strain angle is 0° (armchair direction). The white lines indicate the emergence of rectangular moiré pattern ($\alpha = 90°$), and the blue line shows the 1D pattern ($\alpha = 180°$). c) Variation of α as a function of strain angle and strain magnitude when twist angle is 1.35°. The white line corresponds to the rectangular moiré pattern, where $\alpha = 90°$.

pattern was observed in a nearly 0°-stacked bilayer WSe_2 (sample #1, twist angle of ≈0.1°). The relationship between the period L and the small twist angle θ is estimated by the equation $L \approx a_0/\theta$, where $a_0 = 0.332$ nm represents the lattice constant of monolayer WSe_2.[2] Interestingly, the moiré pattern is not uniform due to the unintentional strain and/or inhomogeneous θ, proving possible lattice distortion by the strain effect from the normal triangular lattice (indicated by the blue triangle) to the deformed rectangular lattice (white triangle).[1,20] In contrast, in the nearly 1°-stacked bilayer WSe_2 (sample #2), we observed a more uniform superlattice (Figure 1d), suggesting that a smaller twist angle is more vulnerable to unexpected inhomogeneity. During the fabrication process of heterostructures, unintended random strain may be introduced. As will be shown later, the smaller the twist angle, the more significantly the moiré superlattice will distort under a given strain magnitude. Additionally, a smaller twist angle corresponds to a superlattice with a longer period, making the distorting effect more pronounced.[20] The estimated θ of sample #2 was ≈1.35° ($L = 14.10 \pm 0.07$ nm, see the Experimental Section).

Because we established a method to visualize the uniform moiré superlattice on flexible substrates, we introduced a strain effect via substrate bending. To understand the effect of substrate bending on the moiré superlattice, we numerically calculated the variation generated by strain (see Note S1 in the Supporting Information). For clarity, we assumed that the strain was uniaxial and applied it to only one of the two monolayers. As the schematic in **Figure 2a** shows, we considered the combined effect of θ, strain magnitude (ε), and strain angle (φ, where 0° corresponds to the orange line, which is the armchair direction of the strained bottom layer) on the moiré superlattice. We described the distortion of the superlattice using three parameters of a moiré unit cell (dashed black line parallelogram): lengths of two moiré basis vectors (L_{m1} and L_{m2}), and the moiré angle (α) between them. First, as illustrated in Figure 2b, to argue the possibility of deformation from triangular to rectangular, we fixed φ at 0° and clarified the variation of α, which is a direct indicator of the superlattice symmetry, depending on ε and θ. The maximal ε and θ were set to 2% and 3°, respectively, to meet experimental feasibility. The blue line in Figure 2b corresponds to $\alpha = 180°$, which implies the existence of 1D moiré superlattices (Figure S4, Supporting Information).[13] Moreover, the white lines correspond to $\alpha = 90°$, which strongly suggests that deformation into a rectangle is experimentally possible. The linearity of the white lines also indicates that a smaller θ leads to a smaller ε required for deformation.

As the next step, to consider the guideline for experiments, we fixed θ at 1.35° and investigated φ dependencies because, as experimentally shown in Figures 1c,d, a smaller θ causes nonuniformity of moiré superlattice. The φ was varied from 0° to 30°, that is, from the armchair direction to the zigzag direction of the strained monolayer. Again, in Figure 2c, the white line corresponds to $\alpha = 90°$, indicating that a rectangular lattice can be achieved with a smaller ε at $\varphi = 30°$ (zigzag direction) than at $\varphi = 0°$ (armchair direction). Therefore, we chose the combination of parameters (θ, ε, φ) ≈ (1.35°, 1%, 30°) as a guideline for the following experiments. It should be noted that these numerical calculations assume that strain is applied to only one of the two monolayers, and in real experiments, we cannot exclude the simultaneous deformation of the two monolayers. However, the assumption of simultaneous two-monolayer deformation requires a much larger ε for the deformation to rectangular lattice (Figures S4, S5, and Note S1, Supporting Information), meaning that (θ, ε, φ) ≈ (1.35°, 1%, 30°) is the minimum condition.

It is important to note that the appearance of a rectangular moiré superlattice does not necessarily indicate the presence of a rectangular monolayer lattice. This is because the formation of a moiré pattern is determined solely by the interference between the two periodic lattices, regardless of the individual lattice geometries. In this case, a strain magnitude of 1% leads to only a very slight deformation of the monolayer lattice, which is negligible in terms of its impact on the overall structure. This subtle distortion is not sufficient to induce significant changes in the underlying monolayer lattice, further supporting the idea that the moiré superlattice's shape arises primarily from the interaction between the two lattices, rather than the geometry of each individual monolayer.

We used sample #2 (the estimated θ is about 1.35°) and, by mounting the substrate on molds, ε and φ were controlled

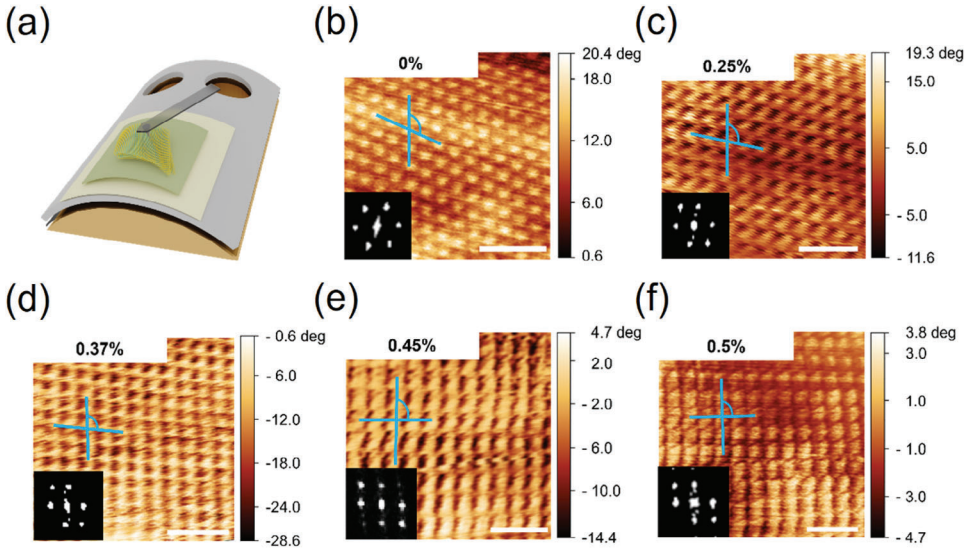

Figure 3. Strain-induced triangular-rectangular moiré superlattice variation. a) Schematic of the experimental setup of PFM measurement on bent substrate. b–f) PFM phase images sample #2 with substrate mounted on molds with flat surface (b), nominal strain = 0%), radius of 25 mm (c), nominal strain = 0.25%), 16.7 mm (d), nominal strain = 0.38%), 13.9 mm (e), nominal strain = 0.45%), and 12.5 mm (f), nominal strain = 0.5%). The blue crosses indicate the variation of the moiré angle α. Scale bars: 50 nm. Insets: FFT images.

(**Figure 3a**).[17,27] For ε, we prepared several molds with different curvatures and tried to control it from 0% (flat) to 0.5% (radius curvature of 12.5 mm) (see the Experimental Section). For φ, we attempted to bend t-BL WSe_2 in the zigzag direction ($\varphi = 30°$) with respect to the zigzag termination boundary of the starting CVD-grown single-crystal monolayer WSe_2.[24,28] As illustrated in Figures 3b–e, we performed PFM measurements for the strained sample #2 and visualized the continuous symmetry modulation of the moiré crystal. Most importantly, as indicated by the angles in the blue crosses, one can identify a continuous variation of the moiré angle from nearly triangular ($\alpha = 120°$) to nearly rectangular ($\alpha = 90°$) with increasing the magnitude of strain. Fast Fourier transform (FFT) images of the superlattice also clearly show a continuous symmetry modulation from triangular to rectangular. After observing the rectangular lattice, we performed a PFM experiment on the unbent (flat) condition and confirmed the reversibility of these deformations (Figure S6, Supporting Information). Note that, even though the substrate was bent during the PFM measurements, the surface of the scanned region remained relatively flat, ruling out the possibility that the distortion of the moiré superlattice was caused by changes in surface flatness (Figure S7, Supporting Information).

To compare the experimental results with the numerical calculations, we directly measured φ using Raman spectroscopy and second-harmonic generation measurements (Figures S8, S9, and Note S2, Supporting Information). The obtained $\varphi = 23°$, which is slightly deviated from 30°. Therefore, the experimental condition for Figure 3f is (θ, ε, φ) ≈ (1.35°, 0.5%, 23°). As shown in Figure 2 and Figure S4 (Supporting Information), the realization of a rectangular moiré under these conditions strongly suggests a high likelihood that strain is applied to only one of the two monolayers. As presented in Figure S4 (Supporting Information), if both layers are strained with the same magnitude, the variation in moiré angle α is significantly smaller, and achieving a rectangular superlattice would require an impractically high strain magnitude. The geometry of the moiré superlattice depends on the interference between the two monolayer lattices (see Note S1 in the Supporting Information). Applying strain to both layers deforms them simultaneously and hardly changes the interference, preventing the superlattice from distorting significantly. Another possibility is that both layers are strained, but with different magnitudes. We calculated this condition by setting the strain magnitude in the top layer as a fraction of that in the bottom layer. The results are shown in Figure S5 (Supporting Information). As expected, increasing the fraction leads to higher strain magnitudes required for rectangular superlattice formation. These conditions require even higher strain magnitudes to distort the moiré superlattice into a nearly rectangular shape. It has also been pointed out that nearly vanishing interlayer friction might emerge in twisted bilayer structure.[29] Therefore, we adopted the model in which only the bottom layer is strained, rather than the one where both layers are strained simultaneously.

Still, there is a discrepancy between the theoretical calculation (θ, ε, φ) ≈ (1.35, 1%, 30°) and the experimental results (1.35°, 0.5%, 23°). The 7° deviation in strain angle is attributed to the sample fabrication process, as we manually stacked the heterostructure and transferred it to the PEN substrate. The strain magnitude also shows a difference, as the experimental strain magnitude for the rectangular pattern is smaller than the theoretical prediction. We attribute this difference to two possible reasons: First, the experimental strain magnitude was determined by the curvature of the bent substrate. However, the localized strain magnitude in the sample might be higher due to surface unevenness, which is difficult to measure. Another possibility is that the theoretical model cannot fully capture the actual strain-induced deformation. When strain is applied, the twist angle might change simultaneously,[30] which goes beyond the assumptions of the model we used. Therefore, to fully understand the

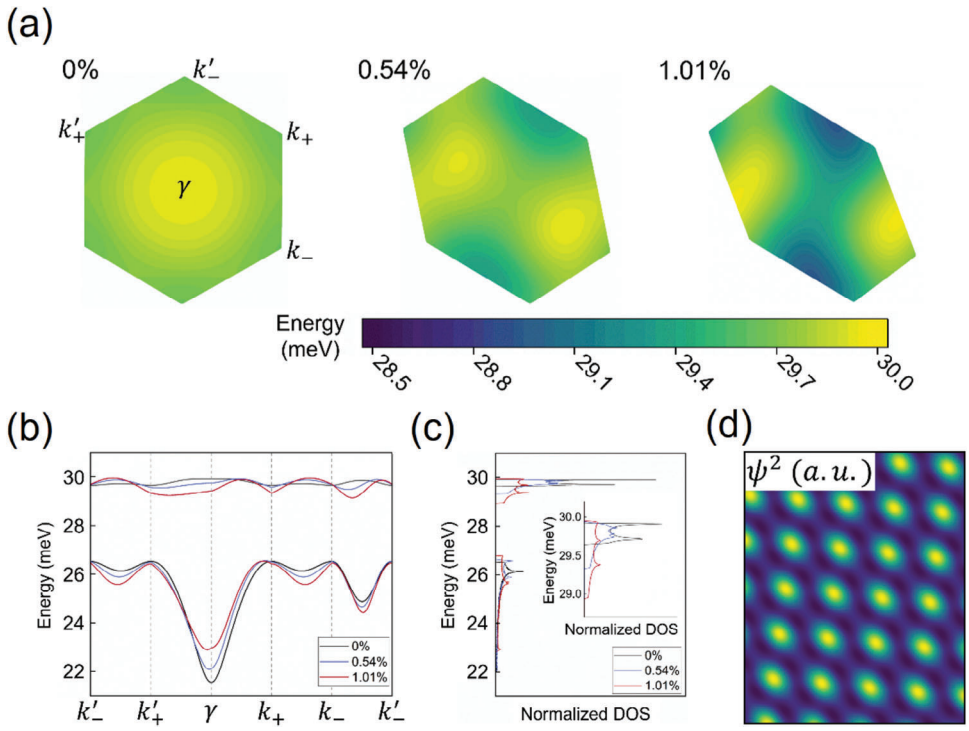

Figure 4. Valence band structure variation in strained twisted bilayer WSe_2. a) Valence band morphology of t-BL WSe_2 when heterostrain is applied with magnitude ε of 0% (left), 0.54% (center), and 1.01% (right). The twist angle and strain angle were fixed at 1.35° and 23°, respectively, in correspondence with the experimental results in Figure 3. b) Band structures of the first two valence bands. c) DOS plots of the first two valence bands. Inset: Magnified DOS plot of the first valence band. d) Spatial distribution of the wave function $|\psi|^2$ at 1.01% strain magnitude.

strain distortion of the moiré superlattice, it is necessary to develop a more comprehensive model. Nevertheless, the presented results have proven that strain can be intentionally introduced to vdW heterostructures to distort the moiré superlattice in the design, which opens the door to studies of combined twist and strain effects on moiré materials.

A previous study showed that the valence band of ≈1° stacked t-BL WSe_2 had a bandwidth of ≈1 meV.[31] To confirm whether this flat-band nature could be sustained in the strained twisted bilayer WSe_2, electronic structure calculations were performed. We adopted an effective continuum model to calculate the band structure variation of the moiré superlattice (Note S3, Supporting Information).[31] The twist angle and strain conditions were set in correspondence to the experimental results $(\theta, \varphi) = (1.35°, 23°)$. Note that because the strain magnitudes are different between calculated and experimental results, the parameters were selected to match the value of α among them (Figure S10m Supporting Information). **Figure** 4a illustrates the variation of the first valence band of the mini Brillouin zone (mBZ) when the moiré angle α is 120°, 106.0°, and 91.5°. The corresponding strain magnitudes were 0%, 0.54%, and 1.01%, respectively. When strain was absent, the mBZ was a normal hexagon, with energy maxima located at γ points and minima at k_+ (k_-) corners.[31] As illustrated in Figures 4b,c, the bandwidth was less than 1 meV, indicating a flat band nature. The application of uniaxial strain (0.54%, center of Figure 4a) distorted the shape of the mBZ and slightly increased its bandwidth (blue line in Figure 4c). More interestingly, within the first mBZ, the energy maximum splits into two peaks, which shift in opposite directions from γ due to symmetry breaking.[11] The energy minima also shift toward the two m points of the mBZ. This redistribution of energy results in a saddle-like morphology around γ.[32,33] As the strain magnitude was further increased (1.01%, right of Figure 4a), the peak splitting became more distinct and the bandwidths were still narrow (≈1 meV at strain of 1.01%), meaning that the anisotropic band structure with a flat-band nature and van Hove singularities (vHSs) can be realized. It can be observed that although the moiré band structure is modified by strain, the band width does not show significant changes. We applied a strain with a magnitude of no more than 1.01% to the bottom layer, which hardly affected its band dispersion.[34] Since the dispersion of the moiré band is determined by both the monolayer band structure and the interlayer coupling-induced moiré potential, the band width remained largely unaffected. However, due to the distortion of the moiré superlattice, the geometry of the moiré potential is tuned, breaking the initial symmetry of the strain-free case and introducing anisotropy into the band structure.

With magnified electron–electron interactions, vHSs are related to many exotic phenomena and new phases of matter because of strengthened instability, such as correlation-induced gap opening and the emergence of superconductivity.[35,36] We show that strain barely affects the bandwidth of the valence band, and the robust vHS in the strained sample allows the observation of correlation-related phenomena. Furthermore, the real-space superlattice exhibited continuous and observable symmetry change, manifesting as high tunability in shape while

maintaining a narrow bandwidth to ensure sufficient correlation. When strain magnitude was 1.01%, the moiré superlattice exhibited a near-rectangular periodicity with highly localized hole wavefunction distribution (Figure 4d). Simultaneously, the strain-induced distortion of the wavefunction was observed, i.e., the anisotropy emerged within the flat-band regime. Thus, we obtained a platform for studying the anisotropic Hubbard model in rectangular superlattices.[37,38] Combined with shape tunability (Figure S11, Supporting Information), the rectangular moiré superlattice in strained t-BL WSe_2 shows tunable anisotropy in both the shape and intercell hopping processes, which makes the material system an ideal fine-tuning quantum simulator for investigating correlation-related phenomena.

In addition, the distorted superlattice symmetry and band structure lead to modifications in optical properties, particularly in the behavior of excitons trapped by the moiré potential, as previously reported.[13] With the established method for applying controllable strain, it is now possible to systematically study the detailed relationship between strain and excitonic behavior through optical measurements. Given the nanometer-scale size of the moiré unit cell, high-resolution techniques, such as tip-enhanced Raman spectroscopy, present a promising direction for future studies.[39] This remains an intriguing aspect and will be a focus of future research.

3. Conclusion

We demonstrated the application of intentional strain to t-BL WSe_2 by fabricating the sample on a flexible substrate. The clear moiré superlattice resolved by PFM proves the feasibility of the proposed structure, in which we successfully realized continuous distortion of the superlattice from triangular to rectangular. We further studied the strain effect on the band structure and revealed an anisotropic band structure with a flat-band nature and vHS. The methods and results of this study pave the way toward the broader utility of 2D vdW heterostructures as highly tunable quantum simulators.

4. Experimental Section

Sample Fabrication: WSe_2 monolayers were grown on SiO_2/Si substrates by CVD process.[24] hBN crystals were purchased from 2D semiconductors and mechanically exfoliated into flakes on a SiO_2 (300 nm)/Si substrate; its thickness was estimated by optical microscopy and determined by atomic force microscopy. The vdW stacks were fabricated using a polymer-assisted transfer method. Two types of polymers were prepared: one was Elvacite 2552C dissolved in anisole (EA. weight ratio 1:1.5), and the other was a mixture of Elvacite with ionic liquid ([EMIM][TFSI]) dissolved in anisole (EIA. weight ratio Elvacite:[EMIM][TFSI]: anisole = 1:0.4:1.5). Prior to sample collection, small drops of both types of polymers were picked and transferred onto glass slides using a toothpick. The slide glasses were then annealed at 180 °C in air for 1 h. EA polymer was first used to pick up hBN flakes at 80 °C. It should be noted that the thickness of the hBN flakes is between 30 and 40 nm, which minimizes the effect of the surface roughness of the Au/Ni film. The hBN was then used to pick monolayer WSe_2. hBN was first put into contact with the monolayer at 90 °C, and the transfer stage was heated to 130 °C to increase the contact area. Subsequently, the monolayer was picked up at 80 °C. The second monolayer was picked afterward, with twist angle control by rotating the transfer stage. The whole stack on EA polymer was then transferred to EIA polymer at 40 °C. At this stage, the bilayer was encapsulated by hBN and the EIA polymer. After transferring the EIA polymer (with the hBN-bilayer stack) onto the substrate, the bilayer was placed on the top for direct PFM measurements. A flexible PEN film (thickness = 125 µm) was first deposited with Ni (2 nm) and Au (10 nm) via vacuum evaporation. The EIA polymer was brought into contact with the substrate at 150 °C, at which the polymer would melt. By removing the substrate from the glass slide, part of the polymer was left on the substrate, with the hBN-bilayer stack buried underneath. The residual polymer was then washed away by sequentially immersing the substrate in chloroform (2 min), acetone (10 min), and IPA (10 min).

PFM Measurements: The moiré pattern of the near-0° bilayer WSe_2 sample #1 was measured using the vertical PFM mode. Annealing was not performed. The horizontal PFM mode was adopted for the near-1° bilayer WSe_2 sample #2. To conduct PFM measurements on the bent substrate mounted on mold, we first sandwiched the PEN substrate between the cap and mold and heated the whole structure at 160 °C for 3 h to fix the shape of the substrate. In order to conduct the PFM measurements, the cap was removed, leaving space for contact between the AFM cantilever and surface of the substrate. To mount the substrate on the mold without a cap, we additionally used the PDMS thin film (thickness = 165 µm) as an adhesion layer. PFM measurements were performed using a Veeco Multimode 8 atomic force microscope in an ambient environment. We used the SCM-PIT-V2 cantilever, which has a force constant of ≈3 N m^{-1}, for all PFM measurements. For the vertical PFM mode measurements, we selected a contact resonance frequency of ≈280 kHz; for the horizontal PFM mode measurements, the contact resonance frequency was set to ≈700 kHz. The applied a.c. bias was between 800 and 2000 mV, and the scan speed of the cantilever was set between 1.5 and 3 Hz for optimal resolution of the acquired images. For all measurements, the contact force was less than 60 nN. The collected data was processed using the Gwyddion software. No background subtraction process was adopted, and the scale range of each image was limited to within 3 × RMS for better visibility of the moiré pattern. The period L in long-period moiré structures with a stacking angle of approximately zero degrees (sample #1) was estimated from the PFM image. It contains a very large error (±43 nm) due to the nonuniform distortion in this sample. On the other hand, the moíre period in sample #2 was estimated by FFT images.[9] To improve the signal-to-noise ratio of the obtained moíre pattern, the raw PFM images were Fourier filtered with a threshold of 70% of the maximum intensity. We further fit the fast Fourier transform satellite peak intensity to a Gaussian function.

Optical Measurements: Raman and photoluminescence spectra were recorded using a JASCO NRS-5100 instrument. The wavelength of the excitation laser was 532 nm through a 100x lens, with a power of 130 µW.

SHG measurements were performed using a home-built optical system with a linearly polarized femtosecond laser (80 MHz) as the excitation source. The wavelength of the laser was fixed at 900 nm, with a power of 730 µW. The second harmonic signal was collected at a wavelength of 450 nm. The angular dependence of the signal was measured by rotating the angle of the excitation laser using a $\lambda/2$ waveplate.

Supporting Information

Supporting Information is available from the Wiley Online Library or from the author.

Acknowledgements

The authors gratefully acknowledge M.S., Y.T., X.T.W., and X.Y.W. for fruitful discussions on the experimental design. This work was financially supported by JSPS KAKENHI Grant Numbers JP20H05867, JP20H05664, JP21H05232, JP21H05234, JP21H05235, JP21H05236, JP22K18986, JP22H00280, JP22H04957, JP22KJ1555, JP22H01899, JP23H05469 and JST, CREST Grant Numbers JPMJCR23A4 and JPMJCR23O3, Japan. H.O. is sponsored by the JSPS Research Fellowship.

Conflict of Interest

The authors declare no conflict of interest.

Data Availability Statement

The data that support the findings of this study are available from the corresponding author upon reasonable request.

Keywords

Moiré superlattice, strain engineering, Transition metal dichalcogenides, van der Waals heterostructures

Received: August 20, 2024
Revised: December 25, 2024
Published online: January 16, 2025

[1] C. N. Lau, M. W. Bockrath, K. F. Mak, F. Zhang, *Nature* **2022**, *602*, 41.
[2] K. F. Mak, J. Shan, *Nat. Nanotechnol.* **2022**, *17*, 686.
[3] I. Bloch, J. Dalibard, S. Nascimbene, *Nat. Phys.* **2012**, *8*, 267.
[4] M. Claassen, L. Xian, A. Georges, A. J. Millis, J. Hone, C. R. Dean, D. N. Basov, A. N. Pasupathy, A. Rubio, *Nat. Phys.* **2021**, *17*, 155.
[5] B.-X. Zheng, C.-M. Chung, P. Corboz, G. Ehlers, M.-P. Qin, R. M. Noack, H. Shi, S. R. White, S. Zhang, G. K.-L. Chan, *Science* **2017**, *358*, 1155.
[6] E. Y. Andrei, D. K. Efetov, P. Jarillo-Herrero, A. H. MacDonald, K. F. Mak, T. Senthil, E. Tutuc, A. Yazdani, A. F. Young, *Nat. Rev. Mater.* **2021**, *6*, 201.
[7] F. Schäfer, T. Fukuhara, S. Sugawa, Y. Takasu, Y. Takahashi, *Nat. Rev. Phys.* **2020**, *2*, 411.
[8] D. M. Kennes, L. Xian, M. Claassen, A. Rubio, *Nat. Commun.* **2020**, *11*, 1124.
[9] K. Kang, W. Zhao, Y. Zeng, K. Watanabe, T. Taniguchi, J. Shan, K. F. Mak, *Nat. Nanotechnol.* **2023**, *18*, 861.
[10] L. Huder, A. Artaud, T. Le Quang, G. T. de Laissardière, A. G. M. Jansen, G. Lapertot, C. Chapelier, V. T. Renard, *Phys. Rev. Lett.* **2018**, *120*, 156405.
[11] Z. Bi, N. F. Q. Yuan, L. Fu, *Phys. Rev. B* **2019**, *100*, 035448.
[12] J.-B. Qiao, L.-J. Yin, L. He, *Phys. Rev. B* **2018**, *98*, 235402.
[13] Y. Bai, L. Zhou, J. Wang, W. Wu, L. J. McGilly, D. Halbertal, C. F. B. Lo, F. Liu, J. Ardelean, P. Rivera, N. R. Finney, X.-C. Yang, D. N. Basov, W. Yao, X. Xu, J. Hone, A. N. Pasupathy, X.-Y. Zhu, *Nat. Mater.* **2020**, *19*, 1068.
[14] M. Huang, Z. Wu, J. Hu, X. Cai, E. Li, L. An, X. Feng, Z. Ye, N. Lin, K. T. Law, N. Wang, *Natl. Sci. Rev.* **2023**, *10*, nwac232.
[15] J. Pu, Y. Yomogida, K.-K. Liu, L.-J. Li, Y. Iwasa, T. Takenobu, *Nano Lett.* **2012**, *12*, 4013.
[16] J. Pu, K. Funahashi, C.-H. Chen, M.-Y. Li, L.-J. Li, T. Takenobu, *Adv. Mater.* **2016**, *28*, 4111.
[17] J. Pu, W. Zhang, H. Matsuoka, Y. Kobayashi, Y. Takaguchi, Y. Miyata, K. Matsuda, Y. Miyauchi, T. Takenobu, *Adv. Mater.* **2021**, *33*, 2100601.
[18] C. Zhang, C.-P. Chuu, X. Ren, M.-Y. Li, L.-J. Li, C. Jin, M.-Y. Chou, C.-K. Shih, *Sci. Adv.* **2017**, *3*, 1601459.
[19] Z. Zhang, Y. Wang, K. Watanabe, T. Taniguchi, K. Ueno, E. Tutuc, B. J. LeRoy, *Nat. Phys.* **2020**, *16*, 1093.
[20] L. J. McGilly, A. Kerelsky, N. R. Finney, K. Shapovalov, E.-M. Shih, A. Ghiotto, Y. Zeng, S. L. Moore, W. Wu, Y. Bai, K. Watanabe, T. Taniguchi, M. Stengel, L. Zhou, J. Hone, X. Zhu, D. N. Basov, C. Dean, C. E. Dreyer, A. N. Pasupathy, *Nat. Nanotechnol.* **2020**, *15*, 580.
[21] K. Yasuda, X. Wang, K. Watanabe, T. Taniguchi, P. Jarillo-Herrero, *Science* **2021**, *372*, 1458.
[22] X. Wang, K. Yasuda, Y. Zhang, S. Liu, K. Watanabe, T. Taniguchi, J. Hone, L. Fu, P. Jarillo-Herrero, *Nat. Nanotechnol.* **2022**, *17*, 367.
[23] S. Masubuchi, M. Sakano, Y. Tanaka, Y. Wakafuji, T. Yamamoto, S. Okazaki, K. Watanabe, T. Taniguchi, J. Li, H. Ejima, T. Sasagawa, K. Ishizaka, T. Machida, *Sci. Rep.* **2022**, *12*, 10936.
[24] N. Wada, J. Pu, Y. Takaguchi, W. Zhang, Z. Liu, T. Endo, T. Irisawa, K. Matsuda, Y. Miyauchi, T. Takenobu, Y. Miyata, *Adv. Funct. Mater.* **2022**, *32*, 2203602.
[25] S. B. Desai, S. R. Madhvapathy, M. Amani, D. Kiriya, M. Hettick, M. Tosun, Y. Zhou, M. Dubey, J. W. Ager III, D. Chrzan, A. Javey, *Adv. Mater.* **2016**, *28*, 4053.
[26] J. Shim, S.-H. Bae, W. Kong, D. Lee, K. Qiao, D. Nezich, Y. J. Park, R. Zhao, S. Sundaram, X. Li, H. Yeon, C. Choi, H. Kum, R. Yue, G. Zhou, Y. Ou, K. Lee, J. Moodera, X. Zhao, J.-H. Ahn, C. Hinkle, A. Ougazzaden, J. Kim, *Science* **2018**, *362*, 665.
[27] H. Ito, Y. Edagawa, J. Pu, H. Akutsu, M. Suda, H. M. Yamamoto, Y. Kawasugi, R. Haruki, R. Kumai, T. Takenobu, *Phys. Status Solidi* **2019**, *13*, 1900162.
[28] Y. Kobayashi, S. Yoshida, M. Maruyama, H. Mogi, K. Murase, Y. Maniwa, O. Takeuchi, S. Okada, H. Shigekawa, Y. Miyata, *ACS Nano* **2019**, *13*, 7527.
[29] G. Ru, W. Qi, K. Tang, Y. Wei, T. Xue, *Tribol. Int.* **2020**, *151*, 106483.
[30] S. Zhu, P. Pochet, H. T. Johnson, *ACS Nano* **2019**, *13*, 6925.
[31] T. Devakul, V. Crépel, Y. Zhang, L. Fu, *Nat. Commun.* **2021**, *12*, 6730.
[32] A. Ziletti, S. M. Huang, D. F. Coker, H. Lin, *Phys. Rev. B* **2015**, *92*, 085423.
[33] Y. Hu, X. Wu, Y. Yang, S. Gao, N. C. Plumb, A. P. Schnyder, W. Xie, J. Ma, M. Shi, *Sci. Adv.* **2022**, *8*, eadd2024.
[34] N. Jena, Dimple, R. A., A. Rawat, M. K. Mohanta, A. De Sarkar, *Phys. Rev. B* **2019**, *100*, 165413.
[35] F, Gebhard, *The Mott Metal-Insulator Transition: Models and Methods*, Springer, Berlin, Heidelberg, **1997**.
[36] R. S. Markiewicz, *Int. J. Mod. Phys. B* **1991**, *05*, 2037.
[37] M. Laubach, R. Thomale, C. Platt, W. Hanke, G. Li, *Phys. Rev. B* **2015**, *91*, 245125.
[38] A. Szasz, J. Motruk, *Phys. Rev. B* **2021**, *103*, 235132.
[39] A. C. Gadelha, D. A. A. Ohlberg, C. Rabelo, E. G. S. Neto, T. L. Vasconcelos, J. L. Campos, J. S. Lemos, V. Ornelas, D. Miranda, R. Nadas, F. C. Santana, K. Watanabe, T. Taniguchi, B. Van Troeye, M. Lamparski, V. Meunier, V.-H. Nguyen, D. Paszko, J.-C. Charlier, L. C. Campos, L. G. Cançado, G. Medeiros-Ribeiro, A. Jorio, *Nature* **2021**, *590*, 405.